

Using the X-ray Dust Scattering Halo of 4U 1624-490 to determine distance and dust distributions

Jingen Xiang¹, Julia C. Lee¹

¹*Harvard-Smithsonian Center for Astrophysics, 60 Garden Street, Cambridge, MA, 02138*

jxiang@cfa.harvard.edu; jcleec@cfa.harvard.edu

and

Michael A. Nowak²

²*Massachusetts Institute of Technology, Chandra X-ray Science Center & Kavli Institute
for Space Research, 77 Massachusetts Ave. NE80-6077, Cambridge, MA, 02139*

mnowak@space.mit.edu

ABSTRACT

We present X-ray dust scattering halo results based on our 76 ks *Chandra* ACIS-S/HETGS observation of the LMXB dipping source 4U 1624-490. Through analysis of the halo light curves with 2-6 keV spectra over the persistent and dipping periods, we estimate a geometric distance of ~ 15 kpc to 4U 1624-490. We also fit halo radial profiles with different ISM dust grain models to assess the location, uniformity, and density of the halo. Our analysis shows that the dust spatial distribution is not uniform along the line-of-sight; rather, it is consistent with the spiral arm structure mapped in HII. The large difference between the absorption Hydrogen column ($N_{\text{H}}^{\text{abs}} \sim 8 \times 10^{22} \text{ cm}^{-2}$; probes all gas along the line-of-sight) derived from broadband spectral fitting, and the scattering Hydrogen column ($N_{\text{H}}^{\text{sca}} \sim 4 \times 10^{22} \text{ cm}^{-2}$; probes only Galactic gas) derived from our studies of the 4U 1624-490 X-ray halo suggests that a large fraction of the column is local to the X-ray binary. We also present (and apply) a new method for assessing the *Chandra* point spread function at large ($> 50''$) angles, through use of the time delays from the observed dips.

Subject headings: dust — scattering — X-rays: ISM — sources: 4U 1624-490

1. Introduction

X-rays are not only absorbed but are also scattered by dust grains when they travel through the interstellar medium (ISM). This scattering of X-rays from a source behind a dust containing cloud in the ISM will lead to the formation of an X-ray scattering halo surrounding the X-ray source. The properties of the halo depend upon the size distribution and density of the dust grains, and on the relative geometry of dust, X-ray source, and observer.

Such dust scattering halos were first discussed by Overbeck (1965), but they were not observationally confirmed until Rolf (1983) observed the X-ray binary GX 339-4 with the *Einstein* X-ray Observatory. Since then, X-ray halos have been studied via observations facilitated by X-ray satellites which include *Einstein*, *ROSAT*, *BeppoSAX*, *Chandra* and *XMM-Newton*. Thus far, the most complete samples of these studies have been presented by Predehl & Schmitt (1995) based on *ROSAT* data, and by Xiang, Zhang & Yao (2005) based on observations with the *Chandra* ACIS-S/HETGS. Of additional note, Draine & Tan (2003) have analyzed *ROSAT* observations of the halo associated with the X-ray nova V1974 Cygni 1992 to confirm that the interstellar dust model of Weingartner & Draine (2001, hereafter WD01) is consistent with the observed X-ray halos. Furthermore, based on *Chandra* ACIS-I observations of the low-mass X-ray binary (LMXB) GX 13+1, Smith, Edgar & Shafer (2002) reported that both the grain model WD01 and the “classical” model of Mathis, Rumpl & Nordsieck (1977, hereafter MRN) can adequately reproduce its halo radial profile.

X-ray halos are not limited to the aforementioned binaries. Most bright X-ray sources are surrounded by X-ray halos (Predehl & Schmitt 1995), including one of the most extreme of the dipping sources, the *Big Dipper* 4U 1624-490, which is an atoll source (Lommen et al. 2005) with an IR counterpart of magnitude $K_s = 18.3$ (Wachter et al. 2005). The presence of a halo in 4U 1624-490 has been surmised via *BeppoSAX* observations, which exhibit a soft excess above its several arcmin PSF (Balucińska-Church et al. 2000). The poor angular resolution of *BeppoSAX*, however, prevents the direct extraction of the halo radial profile at radii less than 100 arcsec, where the halo is much more prominent.

In this paper, we present a focused study of the X-ray halo associated with 4U 1624-490, using the highest resolution (angular and energy) data to date, as afforded by the *Chandra* ACIS-S/HETGS. The ~ 3 hours long duration of the dips (Watson et al. 1985; Smale, Church & Balucińska-Church 2001; Balucińska-Church et al. 2001) and large obscuration of this compact object offer us the unique opportunity to use the time delay of photons arriving from the halo to determine the distance to 4U 1624-490 (§2 for theory and §4.2 for data analysis), and compare with dust grain models to assess composition and density along the line-of-sight (LOS, §4.3). (The large obscuration may be due to the accretion disk

stream impacting the disk. A $\sim 75\%$ obscuration has been reported by Watson et al. 1985 and Church & Balucińska-Church 1995; the superior angular resolution of *Chandra* allows us to detect a 90% obscuration; §4.2.) We also present a new method for assessing the *Chandra* Point Spread Function (PSF) at large angles ($\gtrsim 50''$), and compare the PSF measured by our technique with CHANDRA RAY TRACING (CHART) predictions between 9–160'' (§4.3.1).

2. Theoretical and Historical Background

The theoretical calculations governing the observed halo surface brightness and the time delay of a scattered photon with respect to an unscattered one have been discussed extensively (e.g., Mauche & Gorenstein 1984; Mathis & Lee 1991; Trümper & Schönfelder 1973). Here, we briefly describe the main points.

As discussed by Mauche & Gorenstein (1984), the differential cross section in the Rayleigh-Gans approximation, coupled with the Gaussian approximation for a spherical particle of radius a , can be described by

$$S(a, E, \theta_{sca}) = \frac{d\sigma_{sca}(a, E, \theta_{sca})}{d\Omega} = 1.1 \times 10^{-12} \left(\frac{2Z}{M}\right)^2 \left(\frac{\rho}{2}\right) \left(\frac{a}{\mu m}\right)^6 \left[\frac{F(E)}{Z}\right]^2 \exp(-K^2\theta_{sca}^2), \quad (1)$$

where $K = 0.4575(E/keV)^2(a/\mu m)^2$, and θ_{sca} is the angle of scattering. The mean atomic charge (Z), molecular weight (M , in amu), mass density (ρ) and atomic scattering factor [$F(E)$, from Henke 1981] also factor into the calculation. A photon of wavelength λ will be scattered to a typical angle

$$\theta = \lambda/\pi a \propto E^{-1}. \quad (2)$$

For small angles (several arcmin), we can approximate the observed angle by $\theta \approx (1-x)\theta_{sca}$, where $x = d/D$ is the relative distance defined to be the ratio of the distance from scattering grain to observer (d) over the distance between source and observer (D); see Fig. 1.

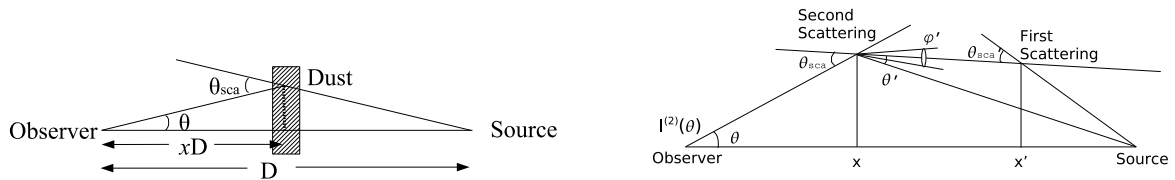


Fig. 1.— Geometry of the X-ray-scattering process for single (left) and double scattering (right).

The intensity of the observed first-order scattering halo, $I_{sca}^{(1)}(\theta, E)$, depends on the X-ray flux $F_X(E)$ of the point source (4U 1624-490 in our case), and is a function of both the observed angle θ and the energy E . The form of this equation, as initially derived by Mathis & Lee (1991), is expressed as

$$I_{sca}^{(1)}(\theta, E) = F_X(E) N_H \int_{a_{min}}^{a_{max}} da n(a) \int_0^1 dx f(x) (1-x)^{-2} \times S\left(a, E, \frac{\theta}{1-x}\right), \quad (3)$$

where N_H is the total hydrogen column density between the observer and the X-ray source, $n(a)$ is the size distribution of the dust grains, and $f(x)$ is the relative hydrogen density to the average total hydrogen density along the LOS at xD . For uniformly distributed dust, $f(x) \equiv 1$, and eq. (3) can take on the more explicit form

$$I_{sca}^{(1)}(\theta, E) \propto F_X(E) N_H \int_{a_{min}}^{a_{max}} da n(a) \left(\frac{a}{\mu m}\right)^6 \frac{\text{erfc}(R)}{R}, \quad (4)$$

where $R = K\theta_{sca} = K(\theta/1-x)$ and $\text{erfc}(R) = (2/\sqrt{\pi}) \int_R^\infty dt \exp(-t^2)$.

Mathis & Lee (1991) further established that multiple scattering is likely important if there is enough scattering optical depth to see an appreciable halo. As discussed by those authors, as well as by Predehl & Klose (1996), for a fixed energy E doubly scattered radiation at the position of the observer can be described via

$$I_{sca}^{(2)}(\theta, E) = F_X(E) N_H \int_0^1 dx f(x) \int_x^1 \frac{dx' f(x')}{(1-x')^2} \int_0^\infty \theta' d\theta' \int_0^{2\pi} d\phi \\ \times \int_{a_{min}}^{a_{max}} da n(a) S(a, E, \theta_{sca}) \times \int_{a_{min}}^{a_{max}} da' n(a') S(a', E, \theta'_{sca}), \quad (5)$$

where

$$\theta_{sca} = \theta'^2 + 2\theta'2 \sin\phi \frac{\theta}{1-x} + \frac{\theta^2}{(1-x)^2}, \quad (6)$$

$$\theta'_{sca} = \theta' \frac{1-x}{1-x'}. \quad (7)$$

For a typical scattering optical depth of $\tau_{sca} \approx 0.5$, the doubly scattered radiation dominates the multiple scattering terms at several arcmin such that higher order (> 2) scatterings can be largely neglected.

Other factors, in particular the ISM dust composition and grain size distribution, affect our overall determination of the halo properties. Several different models exist for describing the composition and size distribution of ISM dust grains. The two most commonly used are the grain model of Weingartner & Draine (2001, WD01), and the ‘‘classical’’ one of

Mathis, Rumpl & Nordsieck (1977, MRN). The details of these two models are different, although they are both based on IR observations. The MRN model assumes both graphite and silicate grains with size distributions: $n(a) \propto a^{-3.5}$, for $a_{min} < a < a_{max}$, where $a_{min} = 0.005 \mu m$ is the same for both grain types, whilst $a_{max} = 0.25 \mu m$ for silicate grains and $a_{max} \approx 0.25 - 1 \mu m$ for graphite grains. In contrast, the WD01 model, which includes very small carbonaceous grains ($a < 0.005 \mu m$) and larger grains ($a > 1 \mu m$), is comparatively more complex than the MRN model. To illustrate, the size of the carbonaceous grains extends to more than $1 \mu m$, while the number of grains decreases sharply with size – see Weingartner & Draine (2001) for details.

3. Observation

We observed 4U 1624-490 on 2004 June 4 (MJD: 53160.26813, ObsID: 4559) with the *Chandra* High Energy Transmission Grating Spectrometer (HETGS) for 76 ks, covering one binary orbit. To reduce pileup, the observation was performed using a reduced 1.7 sec frame-time and one-half sub-array corresponding to 512 columns per CCD. Fig 4 shows that our observation encompasses ~ 2.7 hr total of dipping periods (3 dipping events with durations respectively of about 3.5 ks, 2.3 ks and 4.0 ks).

4. Data Analysis

We used CIAO 3.3 with CALDB 3.2 to extract HETGS spectra of the source for the persistent (non-dipping) and dipping periods (Fig. 4). The 2–6 keV halo light curve between $3''$ and $20''$ is extracted from the CCD S3 0^{th} order data, while the point source light curve in the same energy band is extracted from the dispersed data of the gratings (1^{st} order data). We note that the halo light curve, between $3''$ and $20''$, will have $\sim 40\%$ contamination from the bright point source photons scattered into the wings of the PSF. CIAO 3.3 is also used to extract the surface brightness of the 0^{th} order data for the persistent and dipping periods. (Note that in order to ensure that neither the halo nor the PSF radial profiles are contaminated by the dispersed spectra of the HETGS, throughout we have excluded pie slices of the regions from the zeroth-order image that contain the MEG and HEG arms.) Our analysis technique for the results presented in §4.2 and §4.3 are best illustrated by the flowcharts of Figs. 3 and 5, respectively.

4.1. The broadband spectrum as determined from 1st order HETGS data

In order to determine the distance (§4.2) and distributed Hydrogen column (§4.3) along the LOS to 4U 1624-490, it is necessary that its light curve, and the total flux covering the entire ~ 76 ks spectrum, the dipping phase (~ 12 ks), and persistent phases (persistent 1 + persistent 2, ~ 59 ks) are estimated over the same energy bands. (This corresponds to 2–6 keV over 200 eV incremental steps for this paper; see §4.2 for details.). Furthermore, because there is a direct proportionality between the source spectrum and the X-ray halo intensity such that any uncertainties associated with the spectral analysis will map onto the halo analysis, we take care to use spectra which suffer from the least amount of pile-up in our continuum modeling.

4.1.1. The time averaged continuum covering the binary cycle

The best fit model based on HEG \pm 1 fits to the time-averaged ~ 76 ks spectrum between 1.5-10.0 keV is $1.37_{-0.05}^{+0.08}$ keV blackbody plus $\Gamma = 1.0_{-0.9}^{+0.6}$ power-law modified by $N_{\text{H}} = 7.6_{-0.6}^{+0.9} \times 10^{22}$ cm $^{-2}$. Not surprisingly, these parameters are similar to that derived from the persistent period which is discussed in more depth subsequently.

4.1.2. The persistent phase continuum

The maximal count rate for the HEG \pm 1 spectra during this phase is 7.8×10^{-3} counts per pixel per frame time, corresponding to a maximal pileup $\sim 2\%$ at ~ 5 keV. The maximal count rate per pixel in the MEG \pm 1 is about two times that of HEG \pm 1, indicating a maximal pileup of $\sim 4\%$. Therefore, we have taken care to use the nearly pileup free HEG \pm 1 spectra to derive the flux for the different bands used in our analysis of §4.2 and §4.3. The halo intensity is proportional to E^{-2} such that it decreases sharply with increasing energy. We therefore retain as many low energy (~ 2 keV) halo photons as possible for our halo studies. We further note that we derive broad band spectral parameters based on the 1.5-10 keV spectral region, whilst only the 2-6 keV flux (measured in 200 eV steps) is used in order to match our halo studies of §4.3.

Using ¹ XSPEC 12.2.1 (Arnaud 1996), we fit the broadband source continuum HEG \pm 1 spectrum of the persistent phase with various combinations of powerlaw, blackbody, diskbb

¹<http://heasarc.gsfc.nasa.gov/docs/xanadu/xspec/index.html>

and thermal bremsstrahlung modified by the Tuebingen-Boulder ISM absorption model (Wilms, Allen & McCray 2000). (Because of the high count rate of the source spectrum, the data were binned to require at least 400 counts in each energy bin.) The fitting results are listed in Table 1. We find that both Model 1: absorption×(blackbody+powerlaw) and Model 2: absorption×(diskbb+powerlaw) fit the data well. However, the latter gives an unreasonable photon index of $\Gamma = 12_{-4}^{+8}$, whilst the former agrees better with the parameters reported by Balucińska-Church et al. (2000) based on *BeppoSAX* data, by Smale, Church & Balucińska-Church (2001) based on *RXTE* data, and by Parmar et al. (2002) based on *XMM-Newton* data, barring a flatter photon index in our fitting. The steepness of Γ appears strangely tied to choice of cold absorption model (i.e. WABS versus TBABS), which we will explore in more depth in our forthcoming paper on the high resolution *Chandra* spectrum of 4U 1624-490. For present purposes, it suffices that Model 1 describes the broadband continuum spectrum well (see Fig. 2), such that we can confidently extract flux values over the incremental 200 eV steps between 2-6 keV for our calculations of §4.3.

4.1.3. The dip-phase continuum

We also fit the MEG±1 and HEG±1 spectrum of the dip phase with many of the same models. Due to the lower overall count rate during this phase, we were only able to rebin these data to require $S/N \sim 8 \text{ bin}^{-1}$. Both the MEG±1 and HEG±1 dip spectra are pileup free. We find the best fit for this broad band dip continuum spectrum to be a $\Gamma = 0.7 \pm 0.5$ power-law modified by $N_{\text{H}} = 9.05_{-0.19}^{+0.25} \times 10^{22} \text{ cm}^{-2}$ cold absorption. Fluxes in 200 eV steps were also obtained in the same 2–6 keV energy band to compare with the persistent periods.

4.2. Using the halo and point source light curves to determine distances

The scattering photon travels longer distances than the unscattered one. The delay time dt is given by

$$dt = 1.15 \text{ h } (D/1 \text{ kpc}) (\theta/1 \text{ arcmin})^2 \frac{x}{1-x}, \quad (8)$$

Thus measurement of a time delay between the point source and the halo yields direct information about the distance to the dust cloud and the source. The ~ 3 hr long dipping of 4U 1624-490 provides an excellent opportunity to search for such a delay. Trümper & Schönfelder (1973) and Xu, McCray & Kelley (1986) proposed methods for using this behavior to measure the distance to variable X-ray sources, and Predehl et al. (2000) presented a successful geometric distance determination to Cyg X-3 based on *Chandra* ACIS-S/HETGS observa-

Table 1. Spectral fits to non-dip continuum.

Model	N_{H} (10^{22} cm $^{-2}$)	kT (keV)	Γ	χ^2/dof
blackbody + Power law	$7.8^{+0.8}_{-0.6}$	$1.34^{+0.09}_{-0.05}$	$1.1^{+0.5}_{-1.0}$	364/379
Disk blackbody + Power law	$9.04^{+0.27}_{-0.19}$	2.57 ± 0.06	12^{+7}_{-4}	356/379
Disk blackbody	8.76 ± 0.13	2.64 ± 0.05		373/381
Bremsstrahlung	10.02 ± 0.14	$10.3^{+0.6}_{-0.5}$		442/381
Blackbody	6.60 ± 0.11	1.54 ± 0.02		428/381
Power law	10.77 ± 0.18		1.90 ± 0.04	510/381

Note. — These results come from fits to the *Chandra* ACIS-S/HETGS HEG \pm 1. The MEG \pm 1 is not used since it suffered from more pileup than HEG \pm 1. Errors are 90% confidence. All models listed are modified by the Tuebingen-Boulder ISM absorption model of Wilms, Allen & McCray (2000), as noted in the N_{H} values.

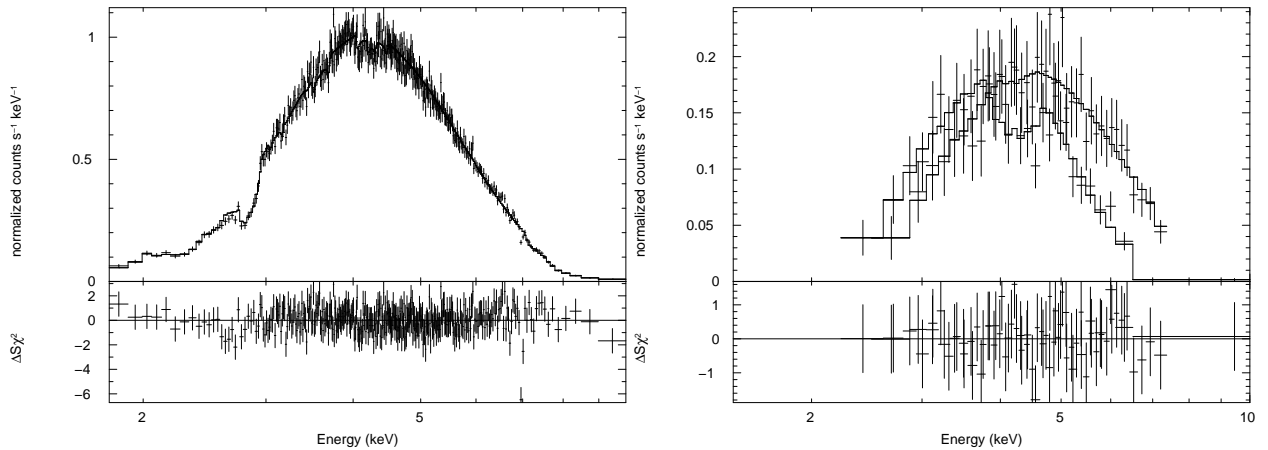


Fig. 2.— The best fit models over-plotted on the broad band spectra of 4U 1624-490 during the persistent phase (HEG \pm 1; left) and dipping periods (HEG \pm 1 and MEG \pm 1; right).

tions.

The time delay dt is only dependent on the location of scattering, but the halo surface brightness is determined by the size, position, and composition of the dust grains, as well as the source flux and scattering hydrogen column. Therefore, the spectrum of the source, the dust grains model and the spatial distribution of the grains is implicitly factored into eq. (8).

The halo intensity is proportional to E^{-2} such that it decreases dramatically at the very high energies. Fig. 2 shows that the majority of the 4U 1624-490 counts are contained within the 2-6 keV energy band. Therefore, we restrict our comparative analysis of the halo and point source light curve exclusively to this band, where fluxes are estimated over 200 eV steps based on the continuum model described in §4.1.1.

In order to avoid pileup effects, the bright point source light curve is extracted directly from the dispersed 1st order data of the HETGS, where the count rate is a factor of ~ 4 lower than that of the non-dispersed 0th order data. In contrast, we extract the (lower flux) halo light curve between 3'' and 20'' from the 0th order data, where the minimum angle is restricted to 3'' to mitigate pileup. We estimate that while pileup at 3'' is less than 2%, between 3''–20'' it is $\ll 1\%$ so that we can safely neglect it for our analysis. The maximum angle restriction of 20'' was chosen to reduce multiple scattering effects, which if not factored in properly can lead to over-predictions of the time delay. Alternatively, we could have restricted the energy band to 3–6 keV, for example. However, this not only would have reduced the degree of multiple scatterings, it would have greatly decreased the halo intensity, which scales as E^{-2} . Thus we opted for the angular restriction with an energy that covers well the observable point source continuum. We estimate that the total halo intensity between 3''–20'' associated with the second-order scattering is less than 5% that of the first-order scattering in the 2-6 keV energy band of interest. While we account for 2nd order scattering effects in our analysis, we wanted to make sure that it would not play a major role in affecting our final results.

A comparison of the halo and point source light-curve (Fig. 4) reveals a mean delay of ~ 1.6 ks for source photons arriving from the halo that is at 3''–20'' from 4U 1624-490. It is interesting to note that the dips we detect show as much as $\gtrsim 90\%$ blockage of the compact object (Fig. 4), compared, for example, to the 75% reported previously in *EXOSAT* (Watson et al. 1985), *Ginga* (Jones & Watson 1989), *BeppoSAX* (Balucińska-Church et al. 2000) and *RXTE* (Smale, Church & Balucińska-Church 2001) observations. This is attributed to the fact that the superior imaging capabilities of *Chandra* can better separate the source light-curve from contaminated light from the halo. Using the time delay, and eq. (8), a simple estimate for the distance to 4U 1624-490 can be derived. If we assume a mean value for the fractional distance: $\bar{x} = \frac{1}{2}$ and a mean effective angle $\bar{\theta} = 10.3''$ derived

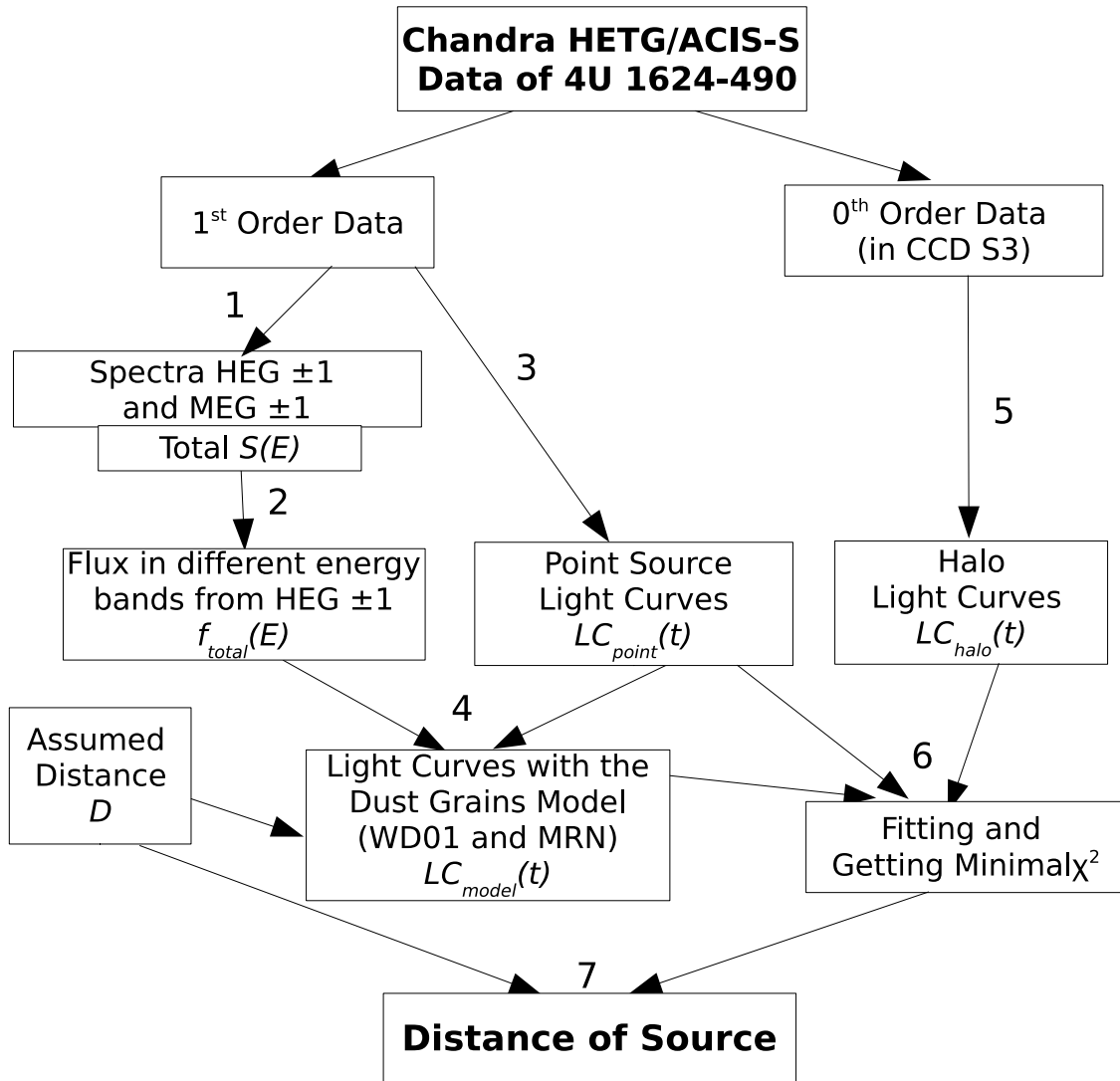


Fig. 3.— Flowchart showing the data analysis process for determining the distance to 4U 1624-490.

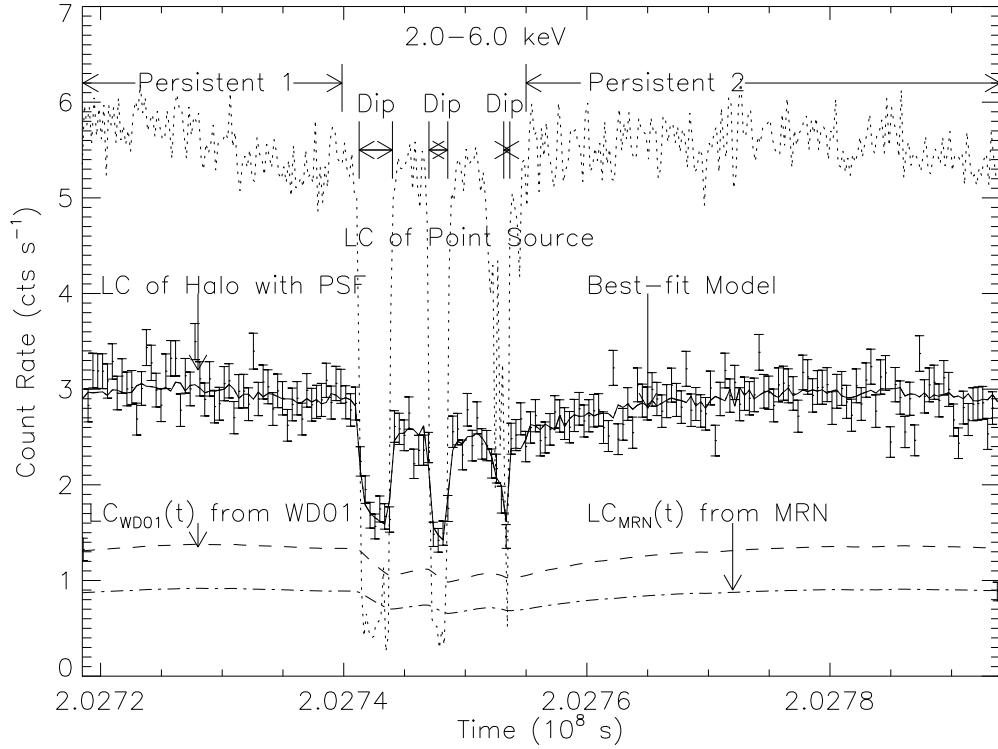


Fig. 4.— The 2–6 keV halo and point source light curves. The top-most dotted line is the point source light curve for 4U 1624-490. The combined halo and PSF light curve between $3''$ and $20''$ is shown, with error bars, in the middle. The overplotted solid line is the “best fit” (χ^2 statistics) for the halo light curve based on $LC_{WD01}(t)$ (dashed line) convolved with the PSF lightcurve. To facilitate clearer viewing, we multiply the observed halo plus PSF light curve by a factor 4, the $LC_{WD01}(t)$ from model WD01 by a factor of 3, and the $LC_{MRN}(t)$ from model MRN by a factor of 2.

using

$$\int_{\theta_{min}}^{\theta_{max}} \theta d\theta \exp \left[-Ka^2 E^2 \left(\frac{\theta}{1-\bar{x}} \right)^2 \right] = \bar{\theta}(\theta_{max} - \theta_{min}) \exp \left[-Ka^2 E^2 \left(\frac{\bar{\theta}}{1-\bar{x}} \right)^2 \right] \quad (9)$$

where $\theta_{min} = 3$ arcsec and $\theta_{max}=20$ arcsec, we obtain a distance to 4U 1624-490 to be about 13.1 kpc. In the subsequent discussion, we discuss a more rigorous approach for deriving the distance.

Following the prescription presented by Predehl et al. (2000), we initially generate model light curves $LC_{WD01}(t)$ (using the WD01 dust model) and $LC_{MRN}(t)$ (MRN dust model) for the halo (Fig. 4), according to eqs. (3) & (8), assuming a uniform spatial distribution of dust, for an initial guess of the distance $D=10$ kpc. [$LC_{WD01}(t)$ and $LC_{MRN}(t)$ will hereafter be referred to generically as $LC_{model}(t)$.] Then we use $LC_{model}(t)$ together with the light curve of the point source $LC_{point}(t)$ to fit the light curve of the halo $LC_{halo}(t)$, allowing for the ratio, $LC_{model}(t):LC_{point}(t)$ to vary until a minimal χ^2 is found. This is iterated for input distances ranging between 8–20 kpc in 0.1 kpc steps. The best fit distance to 4U 1624-490 derived from the WD01 and MRN models for uniformly distributed dust are respectively $D_{WD01} = 15.0^{+2.9}_{-2.6}$ kpc and $D_{MRN} = 10.2^{+2.4}_{-1.4}$ kpc. (Errors are quoted at 90% confidence based on variations in χ^2 with D .) Within errors, both models appear to give consistent values for the distance. However, it may be of interest to note that the distance derived from the MRN model is somewhat sensitive to the allowed maximum size a_{max} for the dust grains. Since the maximum size for carbonaceous grains in the MRN model is not specified, we tried to test our distance determination by changing the maximum size for carbonaceous grains in the MRN model. For $a_{max} = 0.25 \mu\text{m}$, we obtain $D_{MRN} = 10.2^{+2.4}_{-1.4}$ kpc, as noted above, in comparison to $D_{MRN} = 15.0^{+3.0}_{-2.6}$ kpc for $a_{max} = 0.42 \mu\text{m}$ grain sizes. The latter distance estimate is comparable to the value obtained based on the WD01 model.

The WD01 model likely provides a more realistic present day picture of the dust grains in the ISM. Smith, Edgar & Shafer (2002), however, reported that the MRN model is better than the WD01 model in fitting the halo radial profile of GX 13+1, based on observations using the *Chandra* ACIS-I. R. Smith (priv. comm., Dec. 2006) notes, however, that this may be attributable to systematic errors. In a recent reanalysis of GX 13+1, based on a new *Chandra* calibration, Smith finds that the WD01 model may be preferred (although the differences between the WD01 and MRN models are still small). Therefore, for our distance determinations, we are still inclined to accept the value of $D_{4U1624} = 15.0^{+2.9}_{-2.6}$ kpc based on fits using the WD01 model. This is consistent with the 10-20 kpc value derived by Christian & Swank (1997), based on a method which compared the hydrogen column densities from their spectral fitting to an exponential distribution model of hydrogen in the Galaxy.

Furthermore, since dust grains between us and the point source are *unlikely* to be uniformly distributed, we check whether and to what extent our distance determinations are affected by unevenly distributed dust. Accordingly, in our modeling, we vary the dust placement in additional fits, e.g., $x=0.5-1$, $0.4-1$, etc., where $x=0$ and $x=1$ correspond respectively to our position and that of the source (see Fig. 8). We find our distance estimates to be robust to these changes, *as long as* the dust is uniformly distributed *near* the source. This is because the distance estimates are based primarily on small angle scatterings, where the observed halo is attributed primarily to dust near the source (see, e.g., Fig 4 of Mathis & Lee 1991). This finding is consistent with our results based on fits to the halo profile for determining column densities in §4.3.

4.3. Using the halo radial profile to determine the N_{H} spatial distribution

Fits to the halo light curve show that $\sim 40\%$ of the photons come from the point source as far out as $20''$. While *Chandra* has very good imaging resolution, the halo brightness is not much greater than the PSF (see Fig. 7, right). Therefore, a good understanding of the telescope PSF is necessary for optimal results.

4.3.1. The *Chandra* PSF and halo of 4U 1624-490

As discussed by Smith, Edgar & Shafer (2002), the CIAO tool MKPSF and the *Chandra* raytrace model SAOSAC recreate the observed core of the PSF well but underestimate the wings of the PSF. The same is true of the tool CHART since it also uses SAOSAC. Column (d) of Table 2 lists the comparison between the PSF (PSF_{ChaRT}) from the CHART simulation and the one (PSF_{HerX1}) derived from the *Chandra* ACIS-S/HETGS observation of the almost halo-free source, Her X-1 (ObsID 6149). Parameters derived from the Her X-1 observation are used in its CHART simulation. As such, we can confidently use CHART to assess the PSF behavior at small ($\lesssim 50''$) angles. For angles larger than $50''$, we subsequently present a new method for assessing the *Chandra* PSF by using the observed dips in 4U 1624-490.

Fig. 6 shows the WD01 halo model light curve over different angular distances compared against the point source light curve. It is clear that at increasingly larger angles, the flux behavior of the point source is reflected less in the halo light curve (Table 2). This is in part due to a “smearing” effect at large angles as well as the increased delay between the photons arriving from the point source and those arriving from the halo. Capitalizing on this

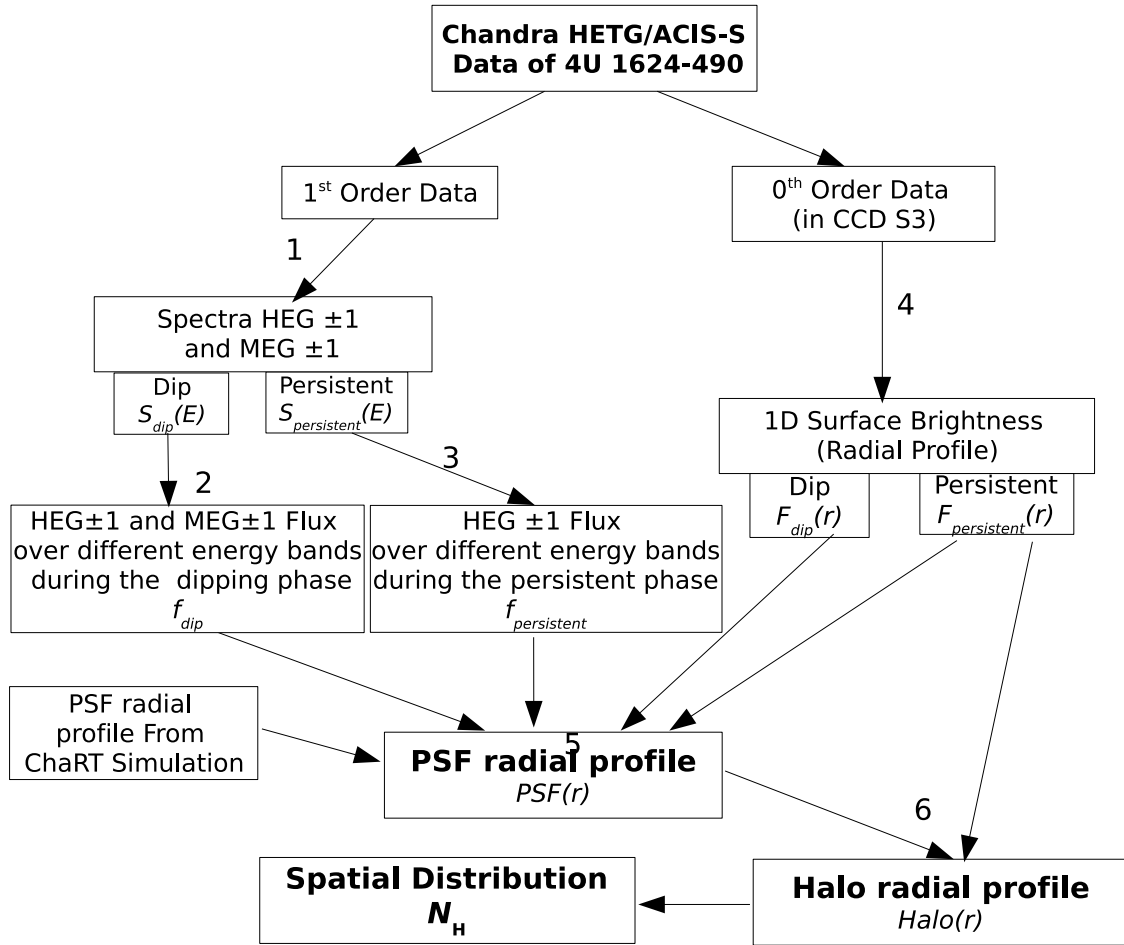


Fig. 5.— Flowchart showing the data analysis process for determining the PSF radial profile and halo radial profile which are used to assess distributions of LOS N_{H} .

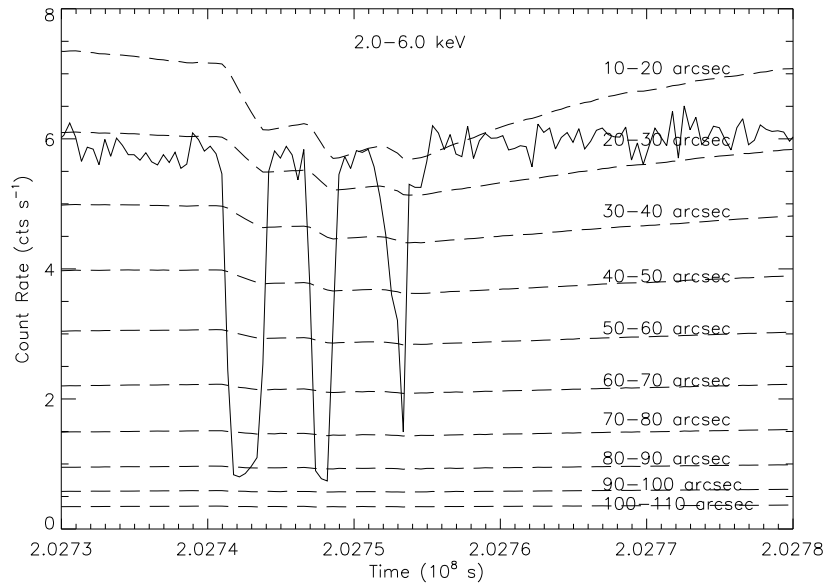


Fig. 6.— The theoretical halo light curves derived from the WD01 model (dashed) at different angular distances based on the observed point source (4U 1624-490) light curve (solid). The halo light curves are arbitrarily multiplied by some constant factor for easier viewing.

observed effect of the dipping phenomenon on the halo light curve, we discuss a prescription for assessing the *Chandra* PSF for 4U 1624-490 at large angles. First we define:

$$PSF(r) = [I_{persistent}(r) - I_{dip}(r)] \frac{F_{persistent}}{(F_{persistent} - F_{dip})}, \quad (10)$$

where $I_{dip}(r)$ and $I_{persistent}(r)$ are respectively, the surface brightness over different radii during the time periods when 4U 1624-490 is dipping and when it is not. Similarly, F_{dip} and $F_{persistent}$ refer to the point source flux during these periods². Based on this, we can then define the surface brightness of the halo :

$$I_{halo}(r) = I_{persistent}(r) - PSF(r) = [I_{dip}(r)F_{persistent} - I_{persistent}(r)F_{dip}] / (F_{persistent} - F_{dip}). \quad (11)$$

To track properly the spectra of the dip and persistent periods and determine how these spectra are reflected in the behavior of the energy dependent PSF, we use eq. (10) to calculate the PSF over the energy range 2–6 keV in 200 eV steps. Note that this equation implicitly assumes no time-dependence of the halo flux. This is, of course, inaccurate, especially at small angular distances from the source. It becomes more accurate, however, at large angular distances where the dipping behavior is “smeared out” in the halo lightcurves (see Fig. 6). Thus, we expect eq. (10) to be less dominated by systematic uncertainties at larger angular distances. Large angular distances are also where CHART estimates of the PSF become more problematic.

To assess the systematic errors in our determination of the PSF radial profile, we use eqs. (3) and (8) to calculate the theoretical halo light curves [$LC_{mod}(t)$] at different ranges of angular distances, as shown in Fig. 6. Specifically, as described in §4.2, we used the lightcurve of the persistent source with different presumed models for the source distance and dust distribution, and chose a model that minimizes the χ^2 for the fit to the halo lightcurves. The halo intensity averaged over the dip phases [i.e., essentially the estimate embodied in eq. (11)] can then be compared to the halo intensity in the persistent phases (i.e., the “true” steady state halo flux). This estimate is presented in column (a) of Table 2. As expected, for radii near the point source, selecting the periods during the dips slightly underestimates the persistent halo flux, and hence leads to a systematic overestimation at small angular radii of the PSF as calculated via eq. (10) [column (c) of Table 2].

²As the halo dips affect the halo surface brightness, especially shortly after the dips, throughout we calculate $I_{persistent}$ solely from persistent phase 1, i.e., the ≈ 20 ksec before the dips. However, for the point source flux, $F_{persistent}$, we use both persistent phases 1 and 2.

As shown in Table 2, for radii $< 50''$, CHART yields less than 13% uncertainties for the PSF, while for radii $> 50''$, using eq. (10) yields uncertainties $< 10\%$ for the PSF. The relative uncertainty in the halo flux is approximately given by the fractional uncertainty in the PSF multiplied by the ratio of the PSF flux to the halo flux [i.e., columns (c) multiplied by column (b) or columns (d) multiplied by column (e) from Table 2]. Thus, by using the CHART PSF estimate for radii $< 50''$, and eq. (10) for radii $> 50''$, the systematic uncertainty in the halo profile should be $< 3\%$ everywhere.

4.3.2. Fits to the halo radial profile

Having gained some understanding of the PSF behavior, we use the WD01 and MRN models to fit the halo radial profile using the fitting codes developed by Smith, Edgar & Shafer (2002), as also applied to the *Chandra* halo studies presented in Xiang, Zhang & Yao (2005). See also Fig. 5 for a flow chart of the analysis process. We confine our halo fitting to angular distributions corresponding to radii $9''$ to $160''$ where the extreme of pileup effect is $< 0.5\%$ at $\gtrsim 9''$ and decreases with angular distance. Therefore, we can assume a pileup free halo for our analysis.

In order to assess dust properties and distribution, for our initial fitting, we assume uniformly distributed dust between $x=0$ (us) and $x=1$ (4U 1624-490; see Fig. 8, as recreated from Caswell & Haynes 1987 and annotated to show the distance of 4U 1624-490 from us). Based on this scenario, we find that neither the MRN model (with $a_{max}(graphite) = 0.42 \mu\text{m}$; $\chi^2/dof = 141/49$ for a best fit $N_{\text{H}} = 4.44^{+0.08}_{-0.08} \times 10^{22} \text{ cm}^{-2}$) nor the WD01 model ($\chi^2/dof =$

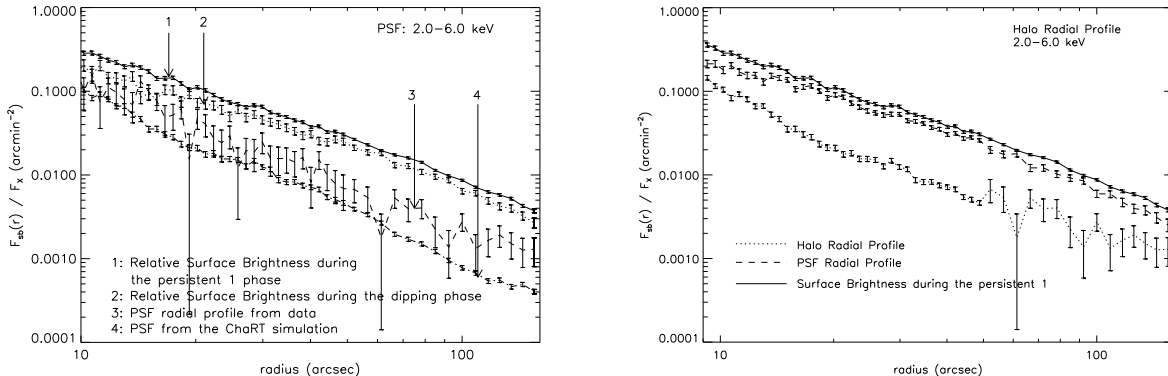


Fig. 7.— PSF (left) and halo (right) radial profile of 4U 1624-490.

Table 2. Estimation of the Systematic Error of PSF and Halo.

radius (")	$\frac{I_{halo}^{wd01,dip}(r) - I_{halo}^{wd01}(r)}{I_{halo}^{wd01}(r)}$ ^a	$\frac{PSF_{data}(r)}{I_{halo}^{data}(r)}$ ^b	$\frac{\Delta PSF_{data}(r)}{PSF_{data}(r)}$ ^c	$\frac{PSF_{HerX1}(r) - PSF_{ChaRT}(r)}{PSF_{HerX1}(r)}$ ^d	$\frac{PSF_{ChaRT}(r)}{I_{halo}^{ChaRT}(r)}$ ^e
09-20	-0.12	0.77	0.18	0.02	0.36
20-30	-0.07	0.51	0.16	0.08	0.23
30-40	-0.05	0.46	0.13	0.13	0.20
40-50	-0.04	0.39	0.11	0.13	0.19
50-60	-0.03	0.32	0.09	0.24	0.16
60-70	-0.02	0.24	0.09	0.30	0.13
70-80	-0.01	0.36	0.04	0.32	0.11
80-90	-0.01	0.25	0.04	0.38	0.11
90-100	-0.003	0.16	0.02	0.46	<0.10
100-160	< -0.003	~0.30	<0.01	> 0.40	<0.10

^a $I_{halo}^{wd01}(r)$ and $I_{halo}^{wd01,dip}(r)$ mean the halo intensity for the persistent and (averaged) dip phases, respectively, derived from fitting the energy-dependent lightcurves with the WD01 model.

^b $PSF_{data}(r)$ is the PSF intensity derived from eq. (10), while $I_{halo}^{data}(r)$ is the halo intensity derived from eq. (11).

^c $\Delta PSF_{data}(r)$ is an estimate of systematic error in the (persistent phase) PSF due to the underestimate of the derived halo intensity [i.e., column (a)]. Specifically, we use the estimate $\Delta PSF_{data}(r)/PSF_{data}(r) \approx [(I_{halo}^{wd01}(r) - I_{halo}^{wd01,dip}(r))/I_{halo}^{wd01}(r)] [F_{persistent}/(F_{persistent} - F_{dip})] [I_{halo}^{data}(r)/PSF_{data}(r)]$.

^d $(PSF_{HerX1} - PSF_{ChaRT})/PSF_{HerX1}$ means the systematic error of PSF intensity from CHART simulations compared with the Her X-1 observational data.

^e $I_{halo}^{ChaRT}(r) = I_{persistent}(r) - PSF_{ChaRT}(r)$ is the halo intensity with the CHART simulation PSF.

Note. — *The data in this table is used solely to discern the relative accuracy of our PSF estimates, and are not used in the calculation of either the PSF or halo radial profiles.*

171/49 with $N_{\text{H}} = 3.40_{-0.06}^{+0.06} \times 10^{22} \text{ cm}^{-2}$) provides good fits to the halo profile. Both models under-predict the halo surface brightness at $>80''$ by $\sim 50\%$. We also fit the halo radial profile to include the second-order scattering and find a 50% substantial improvement in our fits. (We remind the reader that the angular regions probed in this study are much larger than the distance determination study of §4.2, where multiple scattering effects were found to be negligible.) While the fits improved somewhat, they are still statistically unacceptable with $\chi^2/dof \sim 91/49$ for the WD01 model, and $\chi^2/dof \sim 89/49$ for the MRN model of $a_{\text{max}}(\text{graphite}) = 0.42 \mu\text{m}$.

Having determined that the uniformly distributed dust between us and the point source 4U 1624-490 is an unlikely scenario, we investigate whether the models are sensitive to patchy distributions. Accordingly, based on Fig. 8, we roughly divide the dust distribution along our LOS into three parts : $x = 0.0\text{-}0.20$ (Region 1: R1), $0.20\text{-}0.40$ (R2), $0.40\text{-}1.0$ (R3), corresponding to a distance d relative to us of, respectively, $0\text{-}3.0$ kpc (R1), $3.0\text{-}6.0$ kpc (R2), and $6.0\text{-}15.0$ kpc (R3), as seen in Fig. 9. While dust is assumed to be smoothly distributed in each of these regions, the quantity is allowed to vary independently. Based on this, fits to the halo radial profile using the WD01 model yield Hydrogen column densities for each region (Table 3). Compared to fits assuming uniformly distributed dust between $x=0\text{-}1$, $\Delta\chi^2 = 26$ for 47 *d.o.f.* ($\chi^2_{\nu} = 1.38$), i.e., $>99\%$ confidence for 2 additional parameters, according to the F-test. Similarly, fits based on three parts with the MRN model give $\Delta\chi^2 = 24$ for 47 *d.o.f.* ($\chi^2_{\nu} = 1.38$), i.e., again $>99\%$ confidence for 2 additional parameters. The second-order scattering is accounted for in these fits by adding the numerically integrated value of the second-order scattering to the first-order scattering value during fitting of the halo radial profile. The scattering hydrogen column density $N_{\text{HMRN}} = 4.8 \times 10^{22} \text{ cm}^{-2}$ derived from the MRN model is consistent with the result ($N_{\text{H}} = 5.0 \times 10^{22} \text{ cm}^{-2}$ corresponding to $\tau = 2.4$) obtained by Balucińska-Church et al. (2000). We also notice, however, that a smaller $\tau = 1.8$ obtained by Trigo et al (2006) is more consistent with the result $N_{\text{HWD01}} = 3.6 \times 10^{22} \text{ cm}^{-2}$ derived from the WD01 model.

The derived hydrogen column density $N_{\text{HWD01}}^{\text{R1}} = (1.58 \pm 0.15) \times 10^{22} \text{ cm}^{-2}$ (translated into a particle density $n_{\text{R1}} \sim 1.7 \text{ cm}^{-3}$) for the two nearby spiral arms encompassed within R1, is consistent with the result derived from the X-ray halo of Circinus X1 by Xiang, Zhang & Yao

Table 3. Halo fits for deriving N_{H} based on a three parts dust distribution scenario.

Model	$N_{\text{H}}^{\text{R1}} (10^{22} \text{ cm}^{-2})$	$N_{\text{H}}^{\text{R2}} (10^{22} \text{ cm}^{-2})$	$N_{\text{H}}^{\text{R3}} (10^{22} \text{ cm}^{-2})$	$N_{\text{H}}^{\text{tot}} (10^{22} \text{ cm}^{-2})$	$\chi^2/d.o.f$
WD01	1.58 ± 0.15	$0.00_{-0.00}^{+0.18}$	$2.04_{-0.09}^{+0.08}$	$3.62_{-0.06}^{+0.06}$	65/47
MRN	$2.08_{-0.20}^{+0.19}$	$0.00_{-0.00}^{+0.23}$	2.73 ± 0.11	$4.81_{-0.08}^{+0.08}$	65/47

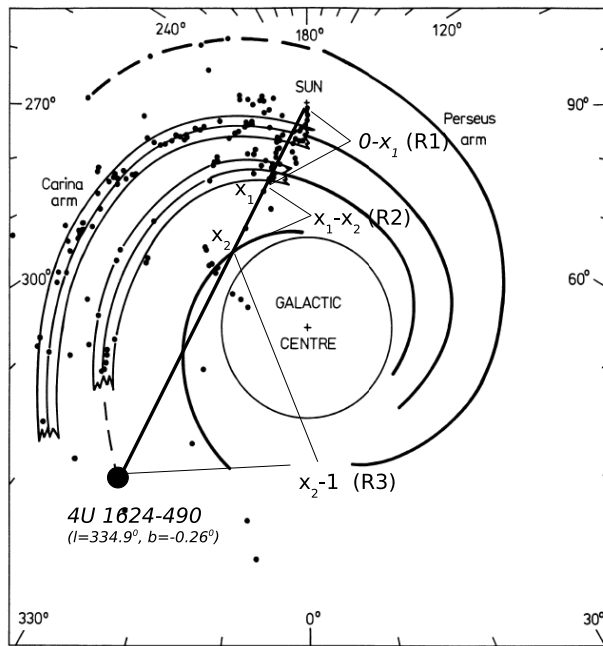


Fig. 8.— The spiral arm structure of the Milky Way Galaxy and the position of 4U 1624-490 in it. The figure is recreated from Caswell & Haynes (1987). The positioning and the source is based on the distance derived in §4.2

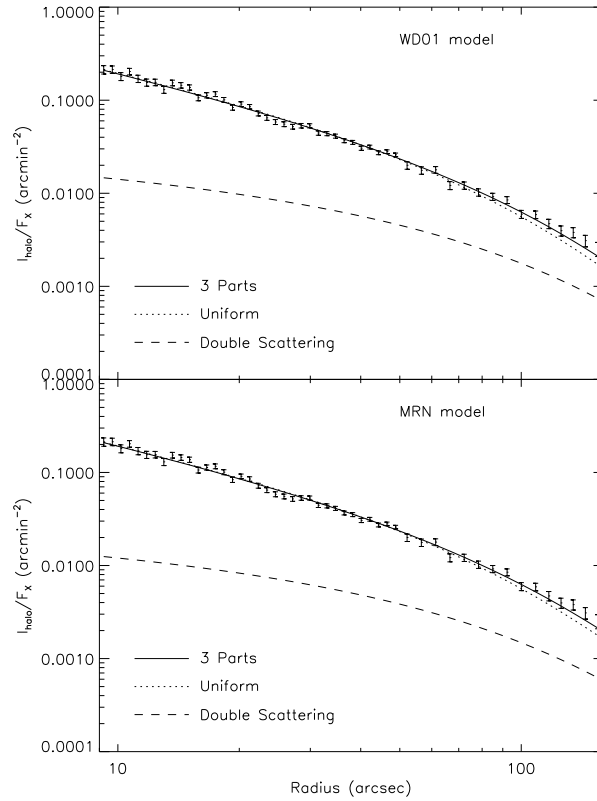


Fig. 9.— X-ray halos observed at 2.0-6.0 keV, fit with dust grains model WD01 (top) and MRN (down). The solid line is the model where the dust spatial distribution is divided into three parts, which is marked in the Fig. 8, and the dotted line is the model with uniformly distributed dust, respectively. The dashed line is the double scattering intensity model with 3 parts dusts.

(2005) over similar distances ($N_{\text{HWD01}}^{\text{CirX-1}} = 1.4 \times 10^{22} \text{ cm}^{-2}$ at ~ 3 kpc from us) along a similar LOS ($l = 322^\circ$, $b = 0.04^\circ$). It should be noted that these two values do not need to be exactly equal since the LOS to 4U 1624-490 and the one to Circinus X-1 pass through different regions of the same two spiral arms. For R2 (the region between spiral arms 2 and 3), we estimate an upper limit to the particle density $n_{\text{R2}} \sim 0.2 \text{ cm}^{-3}$) based on a 90% confidence value for $N_{\text{H}}^{\text{R2}} \leq 1.8 \times 10^{21} \text{ cm}^{-2}$ (Table 3). Combined, the hydrogen particle density in R1 is $n_{\text{R1}} \sim 1.7 \text{ cm}^{-3}$, twice as high as the average density along the entire LOS to 4U 1624-490. The best halo radial profile fits are shown in Fig. 9.

While the absorption hydrogen column density includes both the Galactic ISM and the gas nearby the source, the scattering hydrogen column density only comes from the Galactic interstellar medium. Therefore, our finding that the scattering N_{H} derived independently from the WD01 and MRN models is much less than the absorption N_{H} derived from spectral fitting, implies that there is significant absorption intrinsic to the source. If we naively take the difference between the best fit value $N_{\text{H}}^{\text{abs}} \sim 8 \times 10^{22} \text{ cm}^{-2}$ of the broadband HETGS spectra due to Galactic and source ISM and $N_{\text{H}}^{\text{sca}} \sim 4 \times 10^{22} \text{ cm}^{-2}$ derived from our halo studies, a $N_{\text{H}} \lesssim 4 \times 10^{22} \text{ cm}^{-2}$ can conceivably be local to the source, possibly put there by the stellar wind of the companion.

5. Summary

- We improve upon previous distance estimates for 4U 1624-490 by making use of the delay time of the halo photons relative to the bright point source photons to obtain $D_{4\text{U}1624} = 15.0_{-2.6}^{+2.9}$ kpc. This is consistent within the errors of the 10-20 kpc estimates by Christian & Swank (1997) using a different technique.
- We find that varying dust distributions *will not* affect our distance determination to 4U 1624-490 except possibly for a scenario where there is no dust within ~ 7.5 kpc of the source ($x=0.5-1.0$). This extreme scenario does not match the N_{H} derived from our halo fitting results so it can be ignored as potentially problematic for our distance estimates.
- Using the extreme dipping behavior of 4U 1624-490, we discuss a new method for estimating the *Chandra* PSF at large angles ($> 50''$). In a comparison with CHART estimates for the PSF, we find that if we estimate the PSF using CHART at $< 50''$, and our method at $> 50''$, we can limit the errors associated with our halo analysis to $\lesssim 3\%$ over the angular $9''-160''$ region.
- Varying dust distribution *does* affect the derived column densities. A simple estimate

based on our halo fits imply the hydrogen particle density in the spiral arms is $n_{R1} \sim 1.7 \text{ cm}^{-3}$, and the one between two spiral arms $n_{R2} < 0.2 \text{ cm}^{-3}$.

- For the future, larger field-of-view and high throughput observations combined with on-going *Chandra* studies will allow us to better diagnose the scattering of dust near and far from us to reveal more detailed spatial information.

Note : After submission of this paper, Iaria et al. (2006) posted a preprint presenting the spectral analysis of our HETGS data for 4U 1624-490 which is currently public. Our complete analysis of these data will be presented in a forthcoming publication.

We wish to thank Randall Smith for insightful suggestions. This work was funded by the NASA / *Chandra* grant GO4-3056X – we are thankful for its support. We are also grateful to the Harvard University Clark fund for research support.

REFERENCES

- Arnaud, K. A. 1996, ASPC, 101, 17
- Balucińska-Church M., Humphrey P. J., Church M. J. & Parmar A. N. 2000, A&A, 360, 583
- Balucińska-Church M., Barnard, R., Church, M. J. & Smale, A. P. 2001, A&A, 378, 847
- Caswell J. L. & Haynes F. F. 1987, A&A, 171, 261
- Church M. J. & Balucińska-Church M. 1995, A&A, 300, 441
- Christian D. J. & Swank J. H., 1997, APJS 109, 177
- Draine, B. T., & Tan, Jonathan C. 2003, ApJ, 594, 347
- Henke, B. L. 1981, in Low Energy X-Ray Diagnostics, ed. D. T. Attwood & B. L. Henke (New York: AIP), 146
- Iaria, R. Lavagetto, G. D’Aí, Di Salvo, R. & Robba, N. R. 2006, A&A, astro-ph/0612269
- Jones M. H., & Watson M. G. 1989, in Proc. 23d ESLAB Symp. (ESA SP-296; Paris: ESA), 439
- Lommen, D., van Straaten, S., van der Klis, M. & Anthonisse, B. 2005, A&A, 435, 1005

- Mathis, J. S., Rimpl, W. & Nordsieck, K. H. 1977, *ApJ*, 217, 425 (MRN)
- Mathis, J. S. & Lee, C. W. 1991, *ApJ*, 376, 490
- Mauche, C. W., & Gorenstein, P. 1984, *ApJ*, 302, 371
- Overbeck, J. W. 1965, *ApJ*, 141, 864
- Parmar, A. N., Oosterbroek, T., Boirin, L., & Lumb, D. 2002, *A&A*, 386, 910
- Predehl, P. & Schmitt, J. H. M. M. 1995, *A&A*, 293, 889
- Predehl, P. & Klose, S. 1996, *A&A*, 306, 283
- Predehl, P., Burwitz, V., Paerels, F., & Trümper, J. 2000, *A&A*, 357, L25
- Rolf, D. P. 1983, *Nature*, 302, 46
- Smale, A. P., Church, M. J. & Balucińska-Church M. 2001, *ApJ*, 550, 962
- Smith, R. K., Edgar, R. J., & Shafer, R. A. 2002, *ApJ*, 581, 562
- Trigo, M. D., Parmar, A. N., Boirin, L., Mndez, M., Kaastra, J. S. 2006, *A&A*, 445, 179
- Trümper J., Schönfelder V., 1973, *A&A*, 25, 445
- Wachter, S., Wellhouse, J. W., Patel, S. K., Smale, A. P., Alves, J. F., Bouchet, P. 2005, *ApJ*, 621, 393
- Watson M. G., Willingale R., King, A. R., Gringdlay, J. E., & Halpern, J. 1985, *Space Sci. Rev.*, 40, 195
- Weingartner, J. C. & Draine, B. T. 2001, *ApJ*, 548, 296
- Wilms, J., Allen, A., McCray, R. 2000, *ApJ*, 542, 914
- Xiang, J. G., Zhang, S. N., & Yao, Y. S. 2005, *ApJ*, 628, 769
- Xu. Y., McCray, R., & Kelley, R., 1986, *Nature*, 319, 652